Pion elastic and inelastic scattering from ^{40,42,44,48}Ca and ^{54}Fe

K. G. Boyer,* W. J. Braithwaite, W. B. Cottingame,† S. J. Greene,†
L. E. Smith, and C. Fred Moore
University of Texas at Austin, Austin, Texas 78712

C. L. Morris and H. A. Thiessen
Los Alamos National Laboratory, Los Alamos, New Mexico 87545

G. S. Blanpied‡ and G. R. Burleson
New Mexico State University, Las Cruces, New Mexico 88003

J. F. Davis,§ J. S. McCarthy, and R. C. Minehart
University of Virginia, Charlottesville, Virginia 22901

C. A. Goulding§
Florida A&M University, Tallahassee, Florida 32306
(Received 6 September 1983)

Differential cross sections were measured for pion elastic and inelastic scattering from ^{40,42,44,48}Ca and ^{54}Fe at $T_\pi = 116.0$, 180.0, and 292.5 MeV. Elastic scattering was analyzed using a Kisslinger potential with and without free parameters. The low-lying collective states were analyzed using distorted wave impulse approximation calculations with no free parameters and with transition densities obtained from electron and proton scattering. These calculations adequately reproduced the pion scattering data. Ground-state neutron density root-mean-square radii were estimated.

[NUCLEAR REACTIONS ^{40,42,44,48}Ca($\pi^\pm,\pi^{\pm\prime}$) and ^{54}Fe($\pi^\pm,\pi^{\pm\prime}$); $T_\pi = 116.0$, 180.0, and 292.5 MeV; measured $\sigma(\theta)$; optical-model analysis.]

I. INTRODUCTION

The pion has long been considered a promising probe for obtaining information about the proton and neutron transition densities in nuclear transitions. This promise is derived from the fact that the $\pi^+ + p$ and $\pi^- + n$ elastic scattering amplitudes are three times the corresponding amplitudes for $\pi^+ + n$ and $\pi^- + p$ in the region of the pion-nucleon $\Delta_{3,3}$ ($J = \frac{3}{2}$, $T = \frac{3}{2}$) resonance. One method for testing this promise should involve the comparison of π^+ vs π^- elastic and inelastic scattering data for a suitable series of isotones and isotopes using a model for pion-nucleus scattering which is sensitive to nuclear distributions and successful in reproducing scattering results.

In this work, pion elastic and inelastic scattering data have been obtained from ^{40,42,44,48}Ca and ^{54}Fe to provide a complete set of pion scattering data for studying the $1f_{7/2}$ neutron shell in the $Z=20$ calcium isotopic series and to begin studying the $1f_{7/2}$ proton shell by including the ^{54}Fe nucleus of the $N=28$ isotone series among the targets. The pion energies, 116.0, 180.0, and 292.5 MeV, were chosen in order to have data in the lower energy region of the $\Delta_{3,3}$ resonance, at the $\Delta_{3,3}$ resonance peak, and in the upper energy region of the $\Delta_{3,3}$ resonance. This latter energy is also the upper limit of the energetic pion channel and spectrometer (EPICS) at the Clinton P. Anderson Meson Physics Facility (LAMPF).

The calcium isotopic series has already been the subject of recent pion studies where the ground-state neutron root-mean-square (rms) radius differences have been estimated for ^{40}Ca-^{48}Ca using pion elastic differential cross sections at $T_\pi = 130$, 180, and 230 MeV,[1,2] and for ^{40}Ca-^{44}Ca and ^{40}Ca-^{48}Ca using pionic atoms[3,4] and pion total cross sections.[5] In the present work, the ground-state neutron rms radii are estimated for ^{40,42,44,48}Ca and ^{54}Fe and compared with previous measurements. We also test the effectiveness of the Kisslinger potential with the procedure of Cottingame and Holtkamp[6] for the evaluation of the π-nuclear t matrix over a wide range of energies.

In addition to the data obtained in this work, the present study uses the previously reported cross sections at $T_\pi = 180.0$ MeV for the 0_1^+ and 3_1^- states in ^{40}Ca (Ref. 7) and the 0_1^+, 2_1^+, and 3_1^- states of ^{42,44,48}Ca (Ref. 8) for a comprehensive analysis of the data.

II. DATA ACQUISITION

Data were obtained using the EPICS system[9] at LAMPF, which consists of a momentum-dispersing channel and a high-resolution spectrometer. Position-sensitive, delay-line read-out drift chambers[10] are used to measure the particle positions and angles before and after the spectrometer dipoles. For each event, an on-line computer calculates the incident momentum by projecting the particle trajectory back to the target in order to reconstruct the pion scattering angle and position on the target. The scat-

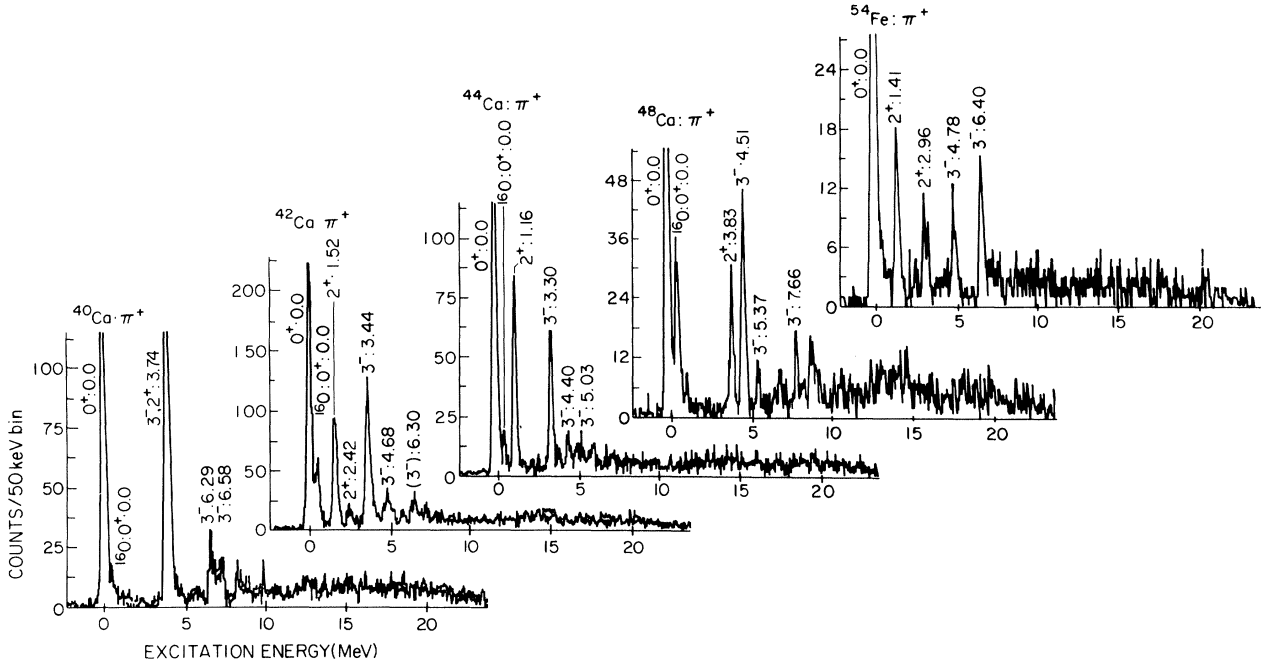

FIG. 1. Typical spectra for ^{40,42,44,48}Ca($\pi^+,\pi^{+\prime}$) and ^{54}Fe($\pi^+,\pi^{+\prime}$) at $T_\pi=180$ MeV and $\theta_{lab}=33°$.

tered pion momentum is then calculated to third order in the particle coordinates. From the scattering angle and the incident and scattered momenta, a Q value at the target is calculated for each event and recorded in Q-value histograms. The spectrometer energy resolution, position resolution at the target, and scattering acceptance angle are 300 keV (FWHM), 3 mm (FWHM), and 10 mrad, respectively.

The data were taken with a channel momentum bite of $\pm 2\%$. At angles less than 20°, the data were taken with a reduced primary beam intensity to obtain an adequately small deadtime in the front chambers. For the data at angles larger than 20°, the pion flux, monitored by two ion chambers 75 cm downstream of the target, was approximately 10^8/s for π^+ and 2×10^7/s for π^-. The two chambers had a 1.0-cm-thick natural iron absorber between them to stop the protons contained in the pion beam.

In order to maximize the resolution of the spectrometer, the data were taken with a reduced spectrometer accep-

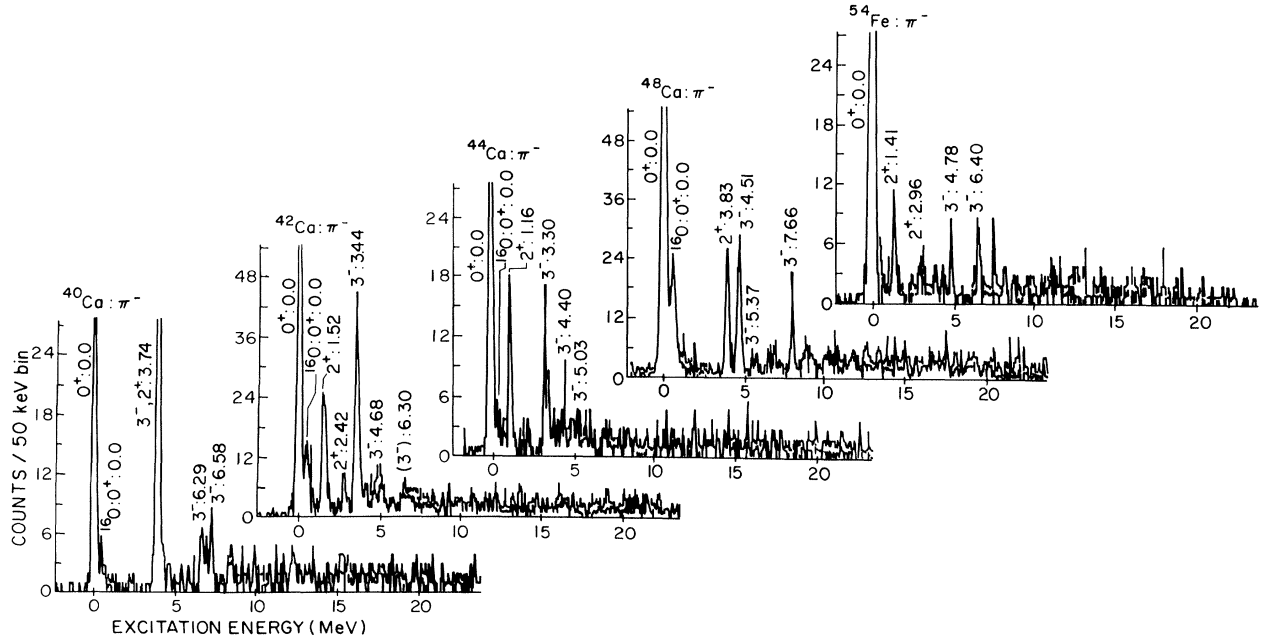

FIG. 2. Typical spectra for ^{40,42,44,48}Ca($\pi^-,\pi^{-\prime}$) and ^{54}Fe($\pi^-,\pi^{-\prime}$) at $T_\pi=180$ MeV and $\theta_{lab}=33°$.

tance angle of 3.0°. This resulted in a spectrometer solid angle of 10 msr. The elastic data were analyzed in 1°-wide scattering angle bins, and the inelastic data in 3°-wide scattering angle bins. The momentum acceptance of the spectrometer was ±6.0%, which allowed a 30 MeV region of excitation energy to be studied in one setting. This acceptance was sufficiently large that only one spectrometer setting at each energy was required for all the angle settings.

Ten isotopically enriched target strips were mounted in a target ladder centered horizontally in separate vertical positions 5 mm apart. The ladder was movable in the vertical direction, corresponding to the dispersion plane of the spectrometer. Five vertically adjacent target strips were examined simultaneously in each of three ladder positions, with the strips arranged such that over the three positions each strip was replaced at least once by ^{40}Ca. Software gates on the vertical target position for each scattered pion separated interactions from the different target strips. The data were sorted into five separate histograms according to the target strip in which the scattering event occurred. Comparisons of the ^{40}Ca($\pi^{\pm},\pi^{\pm}$) histograms indicated the size of the systematic errors arising from changes in the beam momentum and intensity across the five target strips. The variation in the spectrometer solid angle as a function of vertical scattering position in each ladder position was less than 2%. The variation of the cross-section measurements for each isotope as a function of vertical position of the target on the ladder was also less than 2%.

Typical π^+ and π^- Q-value spectra from ^{40,42,44,48}Ca($\pi^{\pm},\pi^{\pm\prime}$) and ^{54}Fe($\pi^{\pm},\pi^{\pm\prime}$) at $\theta_{lab}=33°$ and $T_\pi=180.0$ MeV are presented in Figs. 1 and 2, respectively. States for which data are presented in this paper are listed in Table I. Complete data tables for this experiment may be found in Ref. 11. Also included in Ref. 11 are tables of inelastic cross sections for states not deemed suitable for publication and special $T_\pi=180.0$ MeV ^{40,44,48}Ca($\pi^{\pm},\pi^{\pm}$) and ^{42}Ca(π^-,π^-) elastic scattering angular distribution scans of the first minimum with 0.5°-

TABLE I. States for which data are given in this paper.

	$T_\pi=116.0$ MeV (J^π, MeV)	$T_\pi=180.0$ MeV (J^π, MeV)	$T_\pi=292.5$ MeV (J^π, MeV)
^{40}Ca	0_1^+, 0.000	0_1^+, 0.000[a]	0_1^+, 0.000
	3_1^-, 3.736	3_1^-, 3.736[a]	3_1^-, 3.736
	5_1^-, 4.492		5_1^-, 4.492
	3_2^-, 6.285	3_2^-, 6.285	3_1^-, 6.285
	3^-, 6.58	3^-, 6.58	3^-, 6.58
^{42}Ca		0_1^+, 0.000[b]	0_1^+, 0.000
		2_1^+, 1.524[b]	2_1^+, 1.524
		2_2^+, 2.423	
		3_1^-, 3.444[b]	3_1^-, 3.444
		5_1^-, 4.104	5_1^-, 4.104
		3^-, 4.68	
		(3^-), 6.30	
^{44}Ca	0_1^+, 0.000	0_1^+, 0.000[b]	0_1^+, 0.000
	2_1^+, 1.157	2_1^+, 1.157[b]	2_1^+, 1.157
	3_1^-, 3.308	3_1^-, 3.308[b]	3_1^-, 3.308
		3^-, 4.40	
		3^-, 5.03	
^{48}Ca	0_1^+, 0.000	0_1^+, 0.000[b]	0_1^+, 0.000
	2_1^+, 3.832	2_1^+, 3.832[b]	2_1^+, 3.832
	3_1^-, 4.507	3_1^-, 4.507[b]	3_1^-, 4.507
			3^-, 5.37
		5^-, 5.729	5^-, 5.729
		3^-, 7.66	
^{54}Fe		0_1^+, 0.000	0_1^+, 0.000
		2_1^+, 1.408	2_1^+, 1.408
		2^+, 2.96	
		3^-, 4.78	3^-, 4.78
		3^-, 6.40	

[a]Additional data at $T_\pi=180.0$ MeV for the (0_2^+, 3.352 MeV), (2_1^+, 3.904 MeV), (5_1^-, 4.492 MeV), and (3_3^-, 6.581 MeV) states may be found in Ref. 7. The (0_1^+, 0.000 MeV) and (3_3^-, 6.581 MeV) states are reproduced here from Ref. 7 for comparison.

[b]The 0_1^+, 2_1^+, and 3_1^+ states in ^{42}Ca, ^{44}Ca, and ^{48}Ca have been previously published in Ref. 8.

TABLE II. Ground-state density distribution parameters.

Nucleus	c_p (fm)	a_p (fm)	ω_p	c_n (fm)	a_n (fm)	ω_n	$\langle r^2\rangle_p^{1/2}$ (fm)	$\langle r^2\rangle_n^{1/2}$ (fm)
^{40}Ca	3.42	0.55	0.0	3.42	0.55	0.0	3.40	3.36
^{42}Ca	3.55	0.55	0.0	3.46	0.55	0.0	3.43	3.37
^{44}Ca	3.55	0.55	0.0	3.52	0.55	0.0	3.43	3.41
^{48}Ca	3.47	0.55	0.0	3.63	0.55	0.0	3.38	3.48

wide scattering angle bins.

III. DATA REDUCTION

Peak areas were extracted from the Q-value spectra by using the program LOAF[12] which fitted each spectrum with one of five fixed line shapes corresponding to the isotope represented. The fixed line shape for each isotope was determined by averaging several elastic scattering peaks from spectra in which the oxygen contamination peak was kinematically separated from the elastic peak. Relative separations between the peaks were constrained to values obtained from energy level compilations.[13,14] The background in each spectrum was fit to a polynomial.

The data were normalized to π^+ and π^- scattering on hydrogen using cross sections obtained from the program EDA,[15] which does an energy-dependent reaction matrix analysis of all known pion-hydrogen differential and total cross sections in order to provide energy and angle interpolation. The ratio of the measured pion-hydrogen scattering yields to the predicted EDA $\pi^\pm + p$ cross sections was flat to within $\pm 5\%$ in the angular region between 40° and 90°. The forward-angle ($\theta \leq 20°$) and the larger-angle ($\theta \geq 20°$) data were normalized to each other by running overlap points at 20°.

The data were corrected for chamber efficiency, the fraction of pions which survive the spectrometer flight path, the solid angle as a function of position along the focal plane, and computer live-time. The correction for solid angle was measured by mapping the focal plane using elastic scattering from natural iron at an angle of 38°, which corresponds to the first maximum in the elastic angular distribution. Chamber efficiency and computer live-time were monitored on-line.

Estimated systematic errors in the data sets are the following: chamber efficiency ($\pm 3\%$), survival fraction ($\pm 3\%$), solid angle ($\pm 2\%$), channel bean monitoring ($\pm 3\%$), peak fitting ($\leq 5\%$), and normalization ($\pm 3\%$). The systematic error in the peak fitting arises from the method chosen for fitting the background and uncertainty in the program convergence criteria. The systematic error in the normalization is owing to the error in the pion-hydrogen yield measurements performed during the experiment. The overall normalization uncertainty was $\pm 9\%$ with a relative π^+ vs π^- uncertainty of $\pm 6\%$. Because of background count-rate variations, the chamber efficiencies were found to depend on angle. At the extreme forward angles, systematic angle-dependent deviations as large as $\pm 5\%$ have been seen.

To use the data from all the strips in all the target ladder positions, cross sections from strips of the same isotope were summed over all positions at each angle at each energy. Because each strip has a different central momentum caused by the dispersion of the channel, correcting the central momentum of the strip to the central momentum of the channel is equivalent to shifting the cross-section angles. Using relativistic two-body final-state kinematics,[16] shifted center-of-mass angles were calculated. Because the center-of-mass angle corrections were small, an angular distribution of all the cross sections for a particular isotopic state at a given channel central energy consisted of clusters of points. Each cluster of points was fit with a simple quadratic spline, each point in the cluster was interpolated to the appropriate kinematic center-of-mass angle relative to the channel central energy, and an average cross section with corresponding error was calculated. The net result of this data-reduction correction was a substantial deepening of the minima in the angular distributions over that which was seen when no angular correction had been applied prior to the summation.

An oxygen contamination in the calcium targets was subtracted by fitting the calcium and oxygen elastic scattering peaks separately at all angles greater than 24°. The only other known contamination was a 5% ^{40}Ca con-

TABLE III. Calculated ^{40}Ca b coefficients.

T_π (MeV)	b_{00} Re	b_{00} Im	b_{10} Re	b_{10} Im	b_{01} Re	b_{01} Im	b_{11} Re	b_{11} Im	E_{sh} (MeV)
116.0	−0.67	0.36	−1.40	−0.01	6.83	4.49	3.81	2.23	0.00
	−0.74	0.41	−1.90	−0.04	7.11	2.66	4.05	1.32	−25.00
180.0	−0.58	0.30	−0.96	0.03	3.84	7.41	2.17	3.70	−25.00
292.5	−0.34	0.21	−0.37	0.07	−1.56	1.50	−0.86	0.69	0.00
	−0.44	0.24	−0.54	0.06	−1.99	3.86	−0.96	1.91	−60.00

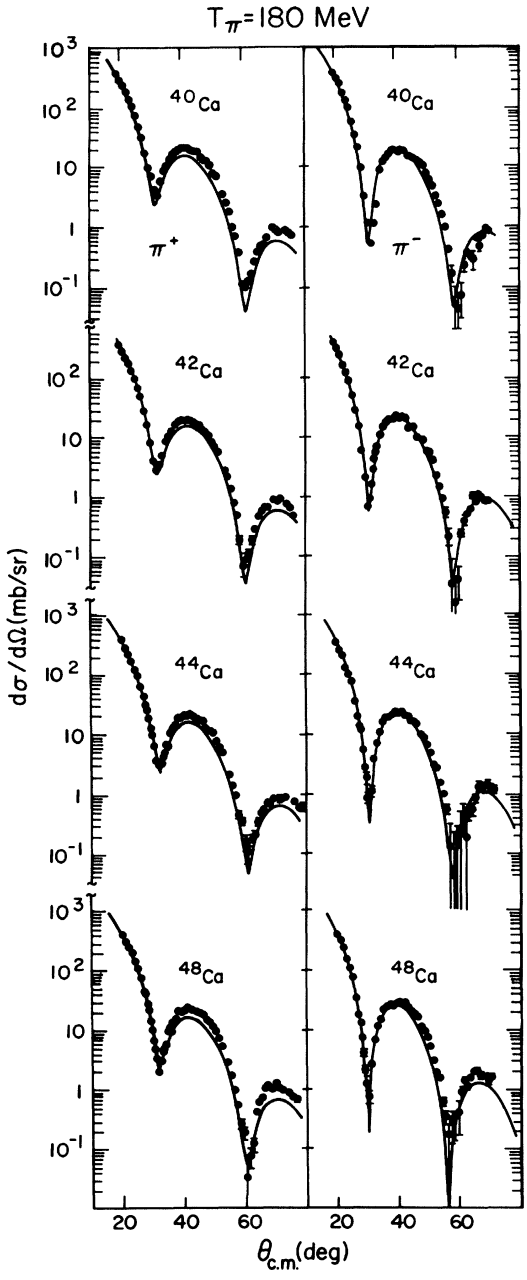

FIG. 3. Angular distributions for ^{40,42,44,48}Ca($\pi^\pm,\pi^\pm$) elastic scattering at $T_\pi=180$ MeV. Optical potential calculations are represented by solid curves.

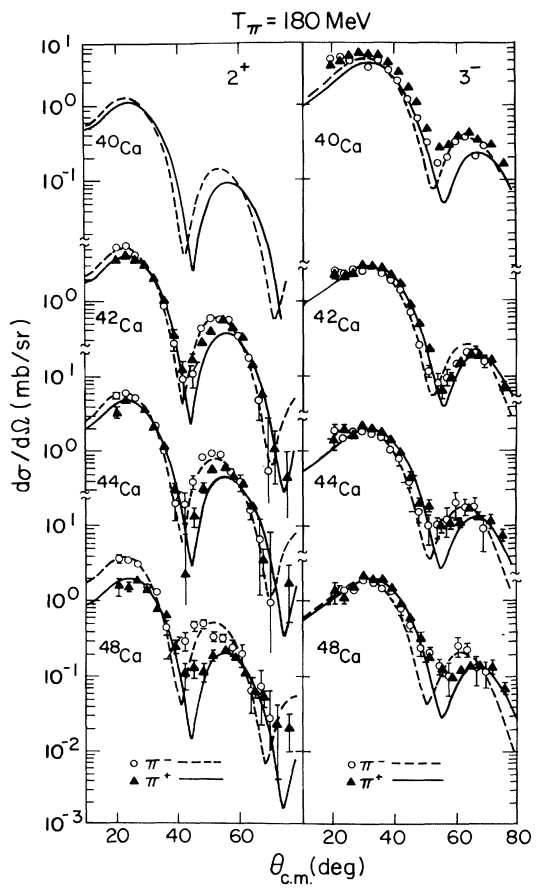

FIG. 4. Angular distributions for ^{40,42,44,48}Ca($\pi^\pm,\pi^{\pm\prime}$) inelastic scattering at $T_\pi=180$ MeV to the first 2^+ and 3^- states. DWIA calculations are represented by solid curves.

tent in the ^{48}Ca target. Consequently, contributions from the (3_1^-, 3.736 MeV) state in ^{40}Ca were subtracted from the (2_1^+, 3.832 MeV) state in ^{48}Ca.

IV. DATA ANALYSIS

A. General remarks

Elastic and inelastic distorted wave impulse approximation (DWIA) calculations were performed with a modified version of the computer code DWPI,[17] which solves a Klein-Gordon equation in coordinate space. The modifi-

TABLE IV. $T_\pi=180.0$ MeV ground-state density distribution fit results.[a]

Nucleus	c_p (fm)	a_p (fm)	ω_p	c_n (fm)	a_n (fm)	ω_n	$\langle r^2\rangle_p^{1/2}$ (fm)	$\langle r^2\rangle_n^{1/2}$ (fm)
^{40}Ca	3.68	0.54	−0.10	3.97±0.02	0.42±0.17	−0.10	3.41	3.39±0.04
^{42}Ca	3.73	0.55	−0.12	3.88±0.03	0.47±0.10	−0.12	3.44	3.40±0.03
^{44}Ca	3.75	0.53	−0.09	4.06±0.03	0.47±0.10	−0.09	3.44	3.55±0.04
^{48}Ca	3.74	0.48	−0.03	4.06±0.04	0.46±0.10	−0.03	3.39	3.57±0.04
^{54}Fe	4.01	0.49	0.0	3.79±0.05	0.57±0.22	0.0	3.60	3.62±0.08

[a] $E_{sh}=-25.0\pm4.0$ MeV

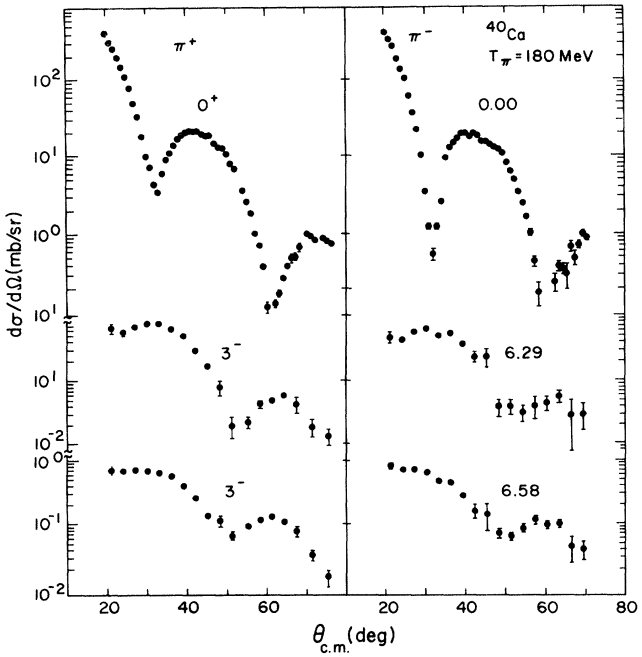

FIG. 5. Angular distributions for $^{40}Ca(\pi^{\pm},\pi^{\pm\prime})$ at $T_\pi=180$ MeV.

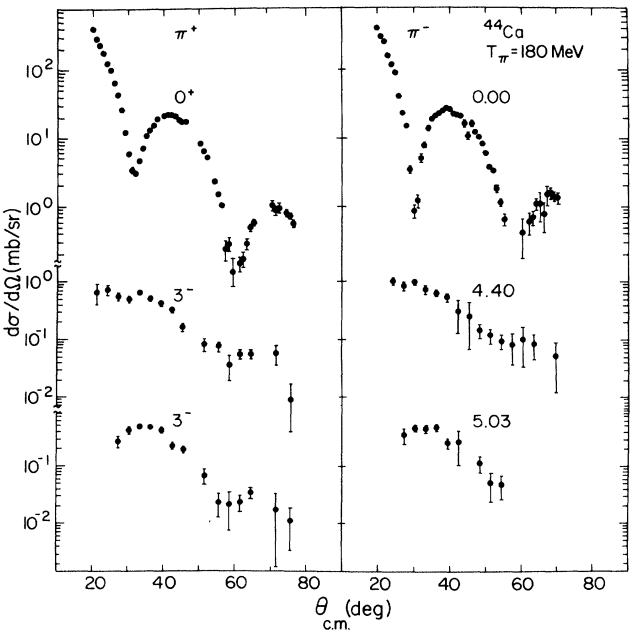

FIG. 7. Angular distributions for $^{44}Ca(\pi^{\pm},\pi^{\pm\prime})$ at $T_\pi=180$ MeV.

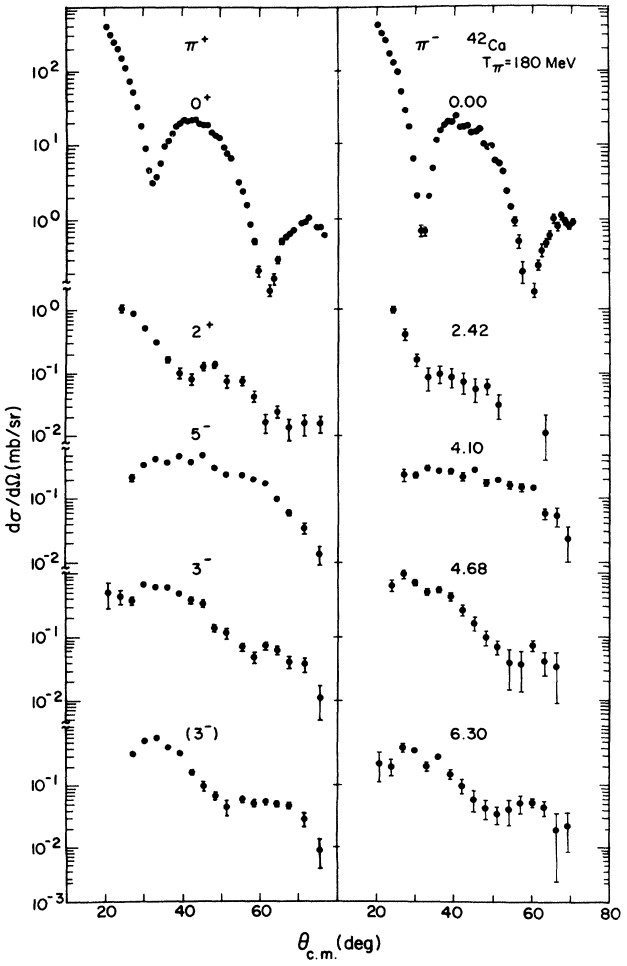

FIG. 6. Angular distributions for $^{42}Ca(\pi^{\pm},\pi^{\pm\prime})$ at $T_\pi=180$ MeV.

cations consisted of (1) incorporating a shift in the energy at which the pion-nucleon phase shifts are evaluated,[6] and (2) tying DWPI to the MINUIT[18] optimizer package. The use of the MINUIT optimizer with DWPI allows any of the DWPI input parameters to be varied while fitting to cross-section data.

All calculations used the Kisslinger form of the optical-model potential,[19]

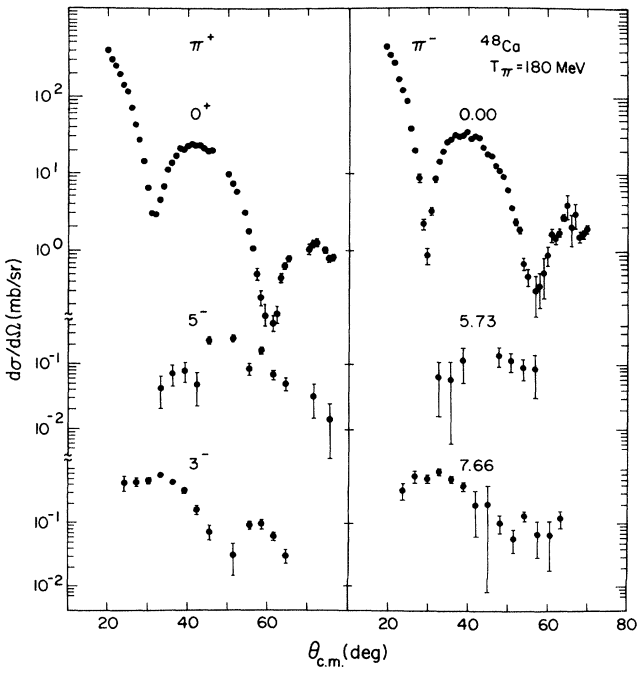

FIG. 8. Angular distributions for $^{48}Ca(\pi^{\pm},\pi^{\pm\prime})$ at $T_\pi=180$ MeV.

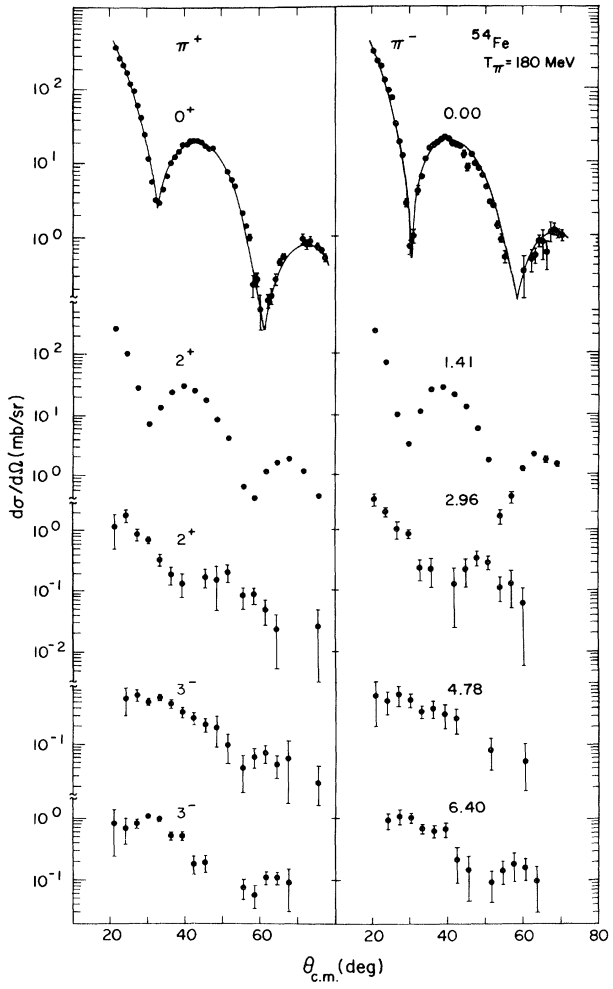

FIG. 9. Angular distributions for ^{54}Fe($\pi^{\pm},\pi^{\pm\prime}$) at $T_\pi = 180$ MeV.

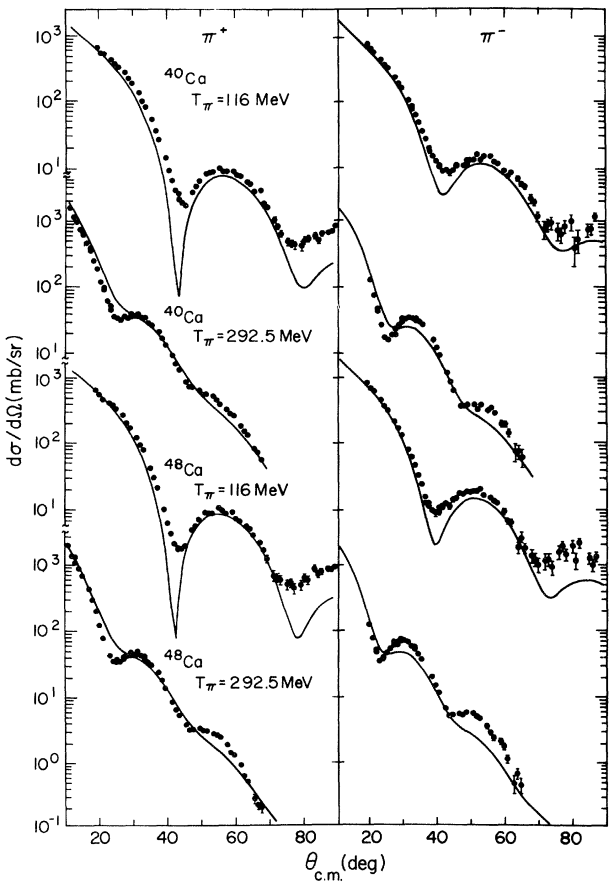

FIG. 10. Angular distributions for ^{40,48}Ca($\pi^{\pm},\pi^{\pm}$) elastic scattering at $T_\pi = 116$ and 292.5 MeV. Optical potential calculations using no energy shifts are represented by solid curves.

$$V(r) = b_{00}k_\pi^2\rho_0(r) + b_{10}\vec{\nabla}\cdot\rho_0(r)\vec{\nabla} - \epsilon_\pi[b_{01}k_\pi^2\rho_1(r) + b_{11}\vec{\nabla}\cdot\rho_1(r)\vec{\nabla}] ,$$

where b_{00}, b_{10}, b_{01}, and b_{11} are related to the pion-nucleon phase shifts,[20] k_π is the pion momentum, ϵ_π is the sign of the pion charge, $\rho_0(r)$ is the isoscalar density distribution

$$[N\rho_n(r) + Z\rho_p(r)]/A ,$$

and $\rho_1(r)$ is the isovector density distribution

$$[N\rho_n(r) - Z\rho_p(r)]/A .$$

The proton- and neutron-density distributions were characterized by a three-parameter Fermi model,

$$\rho(r) = \rho_0(1+\omega r^2/c^2)/\{1+\exp[(r-c)/a]\} .$$

The pion-nucleon phase shifts were evaluated a distance E_{sh} of typically 25 MeV below the actual pion-nucleon center-of-mass energy in the pion-nucleus system. This procedure is the same as that of Cottingame and Holtkamp.[6] It has been successfully applied[6] to nuclei ranging from ^{8}Be to ^{208}Pb over the entire energy range of the $\Delta_{3,3}$ resonance.

TABLE V. $T_\pi = 116.0$ MeV ground-state density distribution fit results.[a]

Nucleus	c_p (fm)	a_p (fm)	ω_p	c_n (fm)	a_n (fm)	ω_n	$\langle r^2\rangle_p^{1/2}$ (fm)	$\langle r^2\rangle_n^{1/2}$ (fm)
^{40}Ca	3.68	0.54	−0.10	3.46±0.03	0.69±0.24	−0.10	3.41	3.56±0.07
^{44}Ca	3.75	0.53	−0.09	3.65±0.07	0.67±0.29	−0.09	3.44	3.65±0.10
^{48}Ca	3.74	0.48	−0.03	3.51±0.04	0.70±0.26	−0.03	3.39	3.72±0.09

[a] $E_{sh} = -25.0\pm4.0$ MeV.

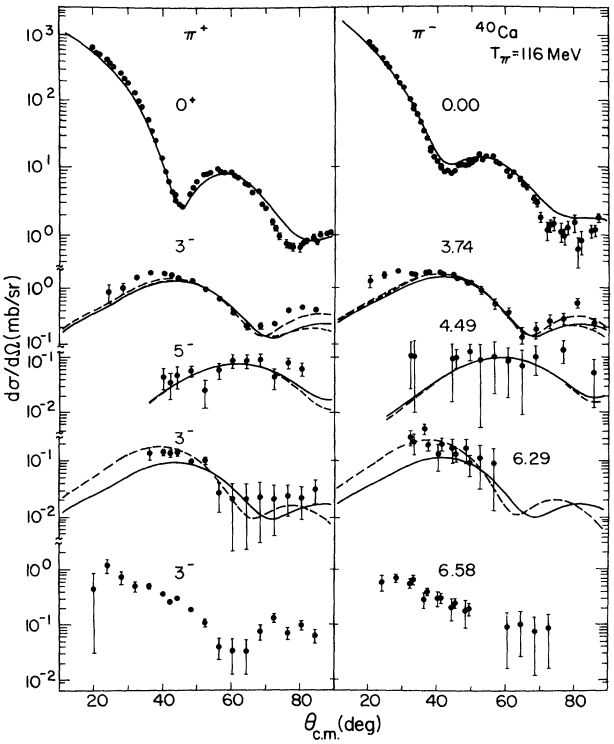

FIG. 11. Angular distributions for ^{40}Ca($\pi^{\pm},\pi^{\pm\prime}$) at T_π=116 MeV. The calculations were done with transition densities from the collective model of Ref. 23 (solid curves), the shell model of Ref. 26 (long-dashed curves), and the Tassie model of Ref. 24 (short-dashed curves).

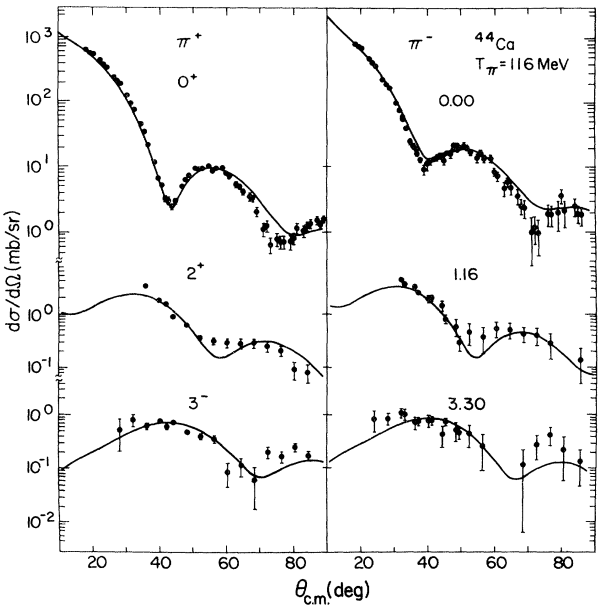

FIG. 12. Angular distributions for ^{44}Ca($\pi^{\pm},\pi^{\pm\prime}$) at T_π=116 MeV. Solid curves as in Fig. 11.

B. T_π=180.0 MeV data

1. Elastic scattering analysis

For the first calcium elastic scattering calculation, the proton and neutron diffusivities a_p and a_n were set to 0.55 fm, and the shape parameters ω_p and ω_n were set to zero. The finite charge size of the proton was unfolded from the nuclear charge distributions measured by elastic electron scattering[21,22] and the half-density radii c_p of the proton point distributions were derived. Then the half-density radii c_n of the neutron point distributions were adjusted to reproduce the location of the first minima in the π^- angular distributions. Table II shows the resulting parameters.

The b coefficients were calculated with a negative energy shift of $E_{sh}=-25.0$ MeV (which is consistent with the energy shift of -30 ± 4 MeV used in Refs. 7 and 8). The results for ^{40}Ca are listed in Table III. The data and resulting calculations for ^{40}Ca are shown in Fig. 3 along with the corresponding data and calculations for ^{42,44,48}Ca reproduced from Ref. 8. This is the first complete exposition of the pion elastic scattering results for the calcium isotope series at T_π=180.0 MeV. The differences between the angular distributions obtained at EPICS and SIN (Refs. 1 and 2) for ^{40,48}Ca at T_π=180.0 MeV are attributed in part to better angular resolution at EPICS.

For the second calcium elastic scattering calculation, the proton and neutron shape parameters ω_p and ω_n were set to the values derived from the elastic electron scattering results. Again the finite charge size of the proton was unfolded from the charge distributions measured by elastic electron scattering and the half-density radii c_p and diffusivities a_p derived. The neutron half-density radii α_n, the neutron diffusivities ω_n, and the energy shift values E_{sh} were then allowed to be freely varied by the optimizer while a fit to the ^{40,42,44,48}Ca data was made. Table IV

TABLE VI. T_π=292.5 MeV ground-state density distribution fit results.[a]

Nucleus	c_p (fm)	a_p (fm)	ω_p	c_n (fm)	a_n (fm)	ω_n	$\langle r^2\rangle_p^{1/2}$ (fm)	$\langle r^2\rangle_n^{1/2}$ (fm)
^{40}C	3.68	0.54	−0.10	3.51±0.02	0.55±0.03	−0.10	3.41	3.32±0.02
^{42}Ca	3.73	0.55	−0.12	3.60±0.05	0.54±0.11	−0.12	3.44	3.33±0.05
^{44}Ca	3.75	0.53	−0.09	3.64±0.07	0.59±0.24	−0.09	3.44	3.49±0.10
^{48}Ca	3.74	0.48	−0.03	4.12±0.03	0.43±0.06	−0.03	3.39	3.55±0.03
^{54}Fe	4.01	0.49	0.0	4.52±0.04	0.40±0.23	0.0	3.60	3.80±0.06

[a]$E_{sh}=-60.0\pm9.0$ MeV.

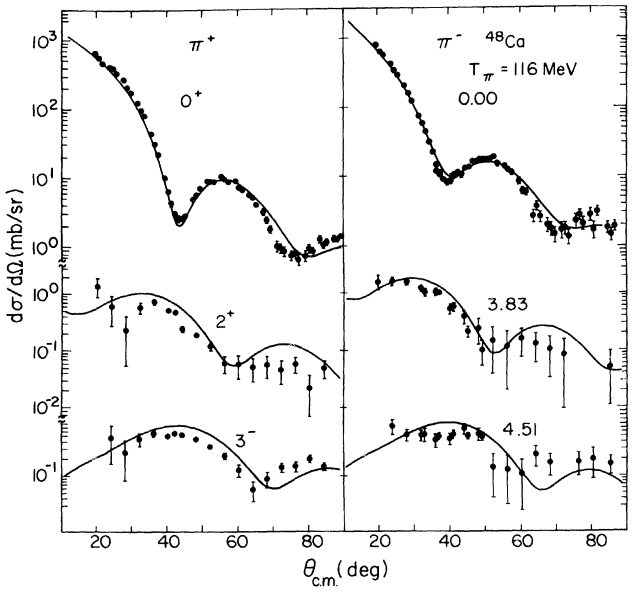

FIG. 13. Angular distributions for $^{48}Ca(\pi^{\pm},\pi^{\pm\prime})$ at $T_\pi = 116$ MeV. Solid curves as in Fig. 11.

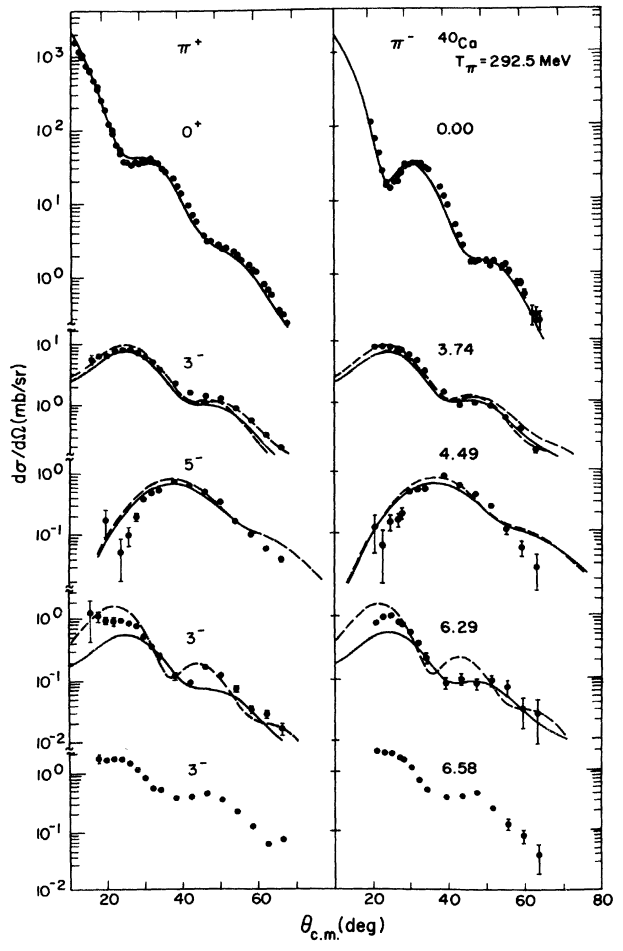

FIG. 14. Angular distributions for $^{40}Ca(\pi^{\pm},\pi^{\pm\prime})$ at $T_\pi = 292.5$ MeV. The calculations were done with transition densities from the collective model of Ref. 23 (solid curves), the shell model of Ref. 26 (long-dashed curves), and the Tassie model of Ref. 24 (short-dashed curves).

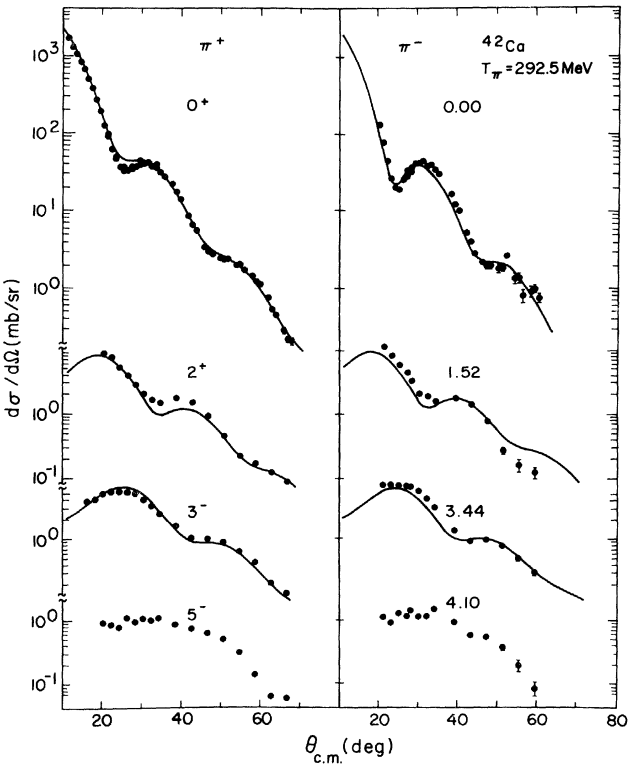

FIG. 15. Angular distributions for $^{42}Ca(\pi^{\pm},\pi^{\pm\prime})$ at $T_\pi = 292.5$ MeV. Solid curves as in Fig. 14.

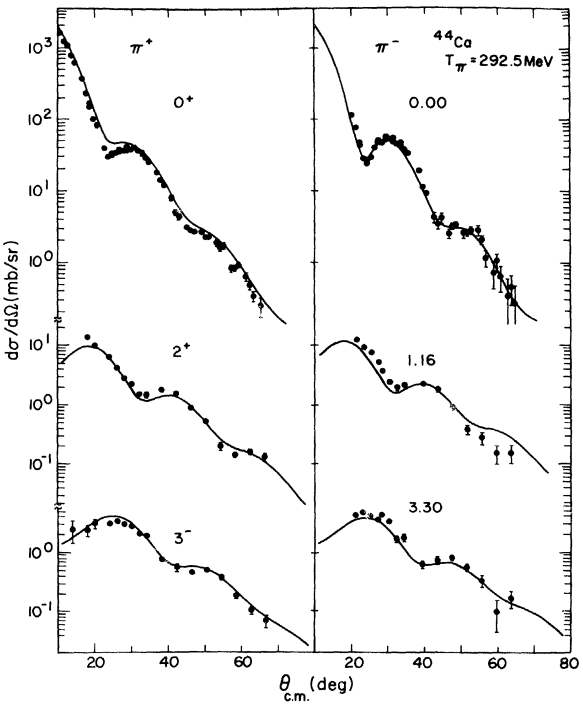

FIG. 16. Angular distributions for $^{44}Ca(\pi^{\pm},\pi^{\pm\prime})$ at $T_\pi = 292.5$ MeV. Solid curves as in Fig. 14.

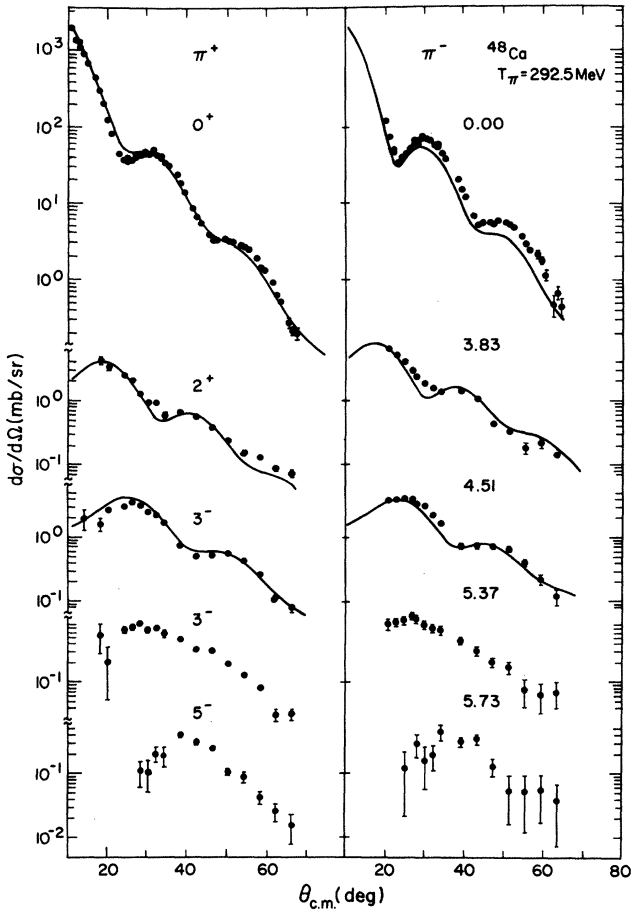

FIG. 17. Angular distributions for $^{48}Ca(\pi^{\pm},\pi^{\pm\prime})$ at $T_\pi=292.5$ MeV. Solid curves as in Fig. 14.

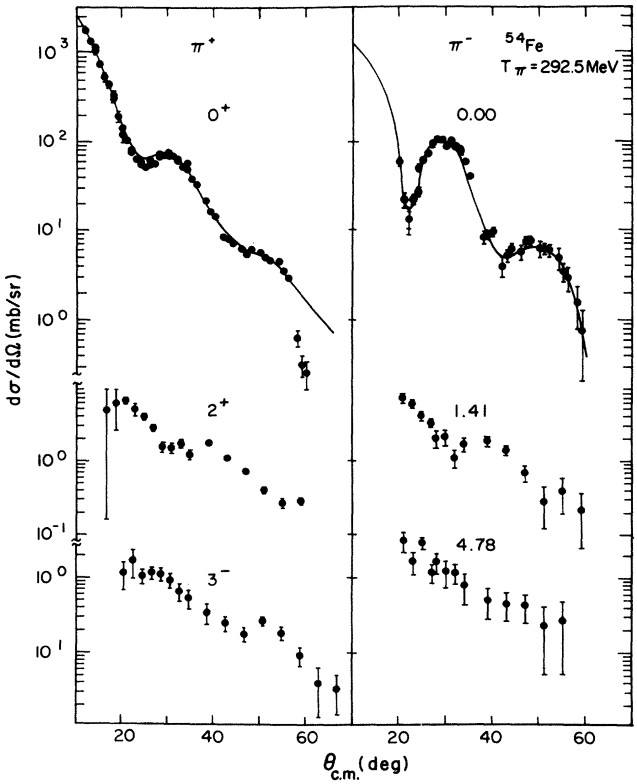

FIG. 18. Angular distributions for $^{54}Fe(\pi^{\pm},\pi^{\pm\prime})$ at $T_\pi=292.5$ MeV. Solid curves as in Fig. 14.

shows the results of the fit corresponding to a final reduced χ^2 of 1.89.

The function provided to the optimizer for use in seeking convergence was the reduced χ^2 which was calculated from all the data sets provided for the fit. The convergence criterion for the optimizer was chosen to be a change in the reduced χ^2 of one. The error for each of the fitted parameters listed in the tables corresponded to one standard deviation.

For the third calculation, a repeat of the second calculation was made but with the inclusion of the ^{54}Fe isotope. The addition of the ^{54}Fe elastic scattering data did not quantitatively affect the fit to the calcium data, and no perceptible change in the shape of the fits from Fig. 3 was observed. Table IV includes the results for ^{54}Fe corresponding to a final reduced χ^2 of 1.95.

2. *Inelastic scattering analysis*

The inelastic scattering calculations were made using the ground-state densities and energy shift given in Table IV. In addition, we used collective-model transition densities for ^{40}Ca obtained from fitting (p,p') data,[23] and mi-

TABLE VII. Neutron rms radii: $\langle r^2\rangle_n^{1/2}$.

	DDHF[a] theory (fm)	(p,p')[b] 0.6, 1.0 GeV (fm)	(α,α')[c] 104 MeV (fm)	This experiment 116.0 MeV (fm)	180.0 MeV (fm)	292.5 MeV (fm)
^{40}Ca	3.36	3.38±0.04	3.34±0.03	3.56±0.07	3.39±0.04	3.32±0.02
^{42}Ca	3.44	3.42±0.04	3.42±0.03		3.40±0.03	3.33±0.05
^{44}Ca	3.50	3.49±0.05	3.48±0.03	3.65±0.10	3.55±0.04	3.49±0.10
^{48}Ca	3.59	3.58±0.04	3.63±0.04	3.72±0.09	3.75±0.04	3.55±0.03

[a]Obtained from Ref. 28 using a density-dependent Hartree-Fock calculation.
[b]Obtained from Ref. 29.
[c]Obtained from Ref. 30.

TABLE VIII. Neutron minus proton rms radii: $\langle r^2\rangle_n^{1/2}-\langle r^2\rangle_p^{1/2}$.

	DDHF[a] theory (fm)	(α,α')[b] 104 MeV (fm)	This experiment 116.0 MeV (fm)	180.0 MeV (fm)	292.5 MeV (fm)
^{40}Ca	−0.04	−0.051	0.15±0.07	−0.02±0.04	−0.09±0.02
^{42}Ca	0.02	−0.002		−0.04±0.03	−0.11±0.05
^{44}Ca	0.08	0.037	0.21±0.10	0.11±0.04	0.05±0.10
^{48}Ca	0.18	0.226	0.33±0.09	0.18±0.04	0.16±0.04

[a]Obtained from Ref. 28 using a density-dependent Hartree-Fock calculation.
[b]Obtained from Ref. 30.

croscopic transition densities for ^{42,44}Ca obtained from fitting inelastic electron scattering data with a Gaussian model[24] and for ^{48}Ca from fitting with a Tassie model.[25] As differences in the neutron and proton distributions were found to be small (Sec. IV B 1), the transition densities were equated for the analysis of the inelastic data. This was also done previously in the fit to the data at 180.0 MeV in Refs. 7 and 8. The strength parameters β_p and β_n for the proton and neutron distributions were adjusted to fit the forward part of the angular distributions. Figure 4 shows the data and resulting calculations for the first 2^+ and 3^- states. Note that because of the limited energy resolution, the 2_1^+ state in ^{40}Ca could not be reliably separated from the 3_1^- state.

All inelastic calcium data not previously published are shown in Figs. 5—8. Elastic data are included in these figures for comparison and calculations are omitted for visual clarity. Figure 9 shows the ^{54}Fe$(\pi^\pm,\pi^{\pm\prime})$ data. Because this isotope has not been extensively analyzed, only an elastic calculation based on Table IV is shown.

C. $T_\pi=116.0$ and 292.5 MeV data

1. *Elastic scattering analysis*

As in the case for the $T_\pi=180.0$ MeV elastic scattering data, a multiparameter fit was made for each of the $T_\pi=116.0$ and 292.5 MeV data sets to determine the corresponding neutron half-density radii α_n, neutron diffusivities ω_n, and energy shift. The results are given in Tables V and VI. The final reduced χ^2 values are 2.09 and 2.04, respectively.

To demonstrate the effect of the energy shift to the π-N t matrix on the quality of the fit to the elastic scattering data, calculations with no energy shifts were made for the $T_\pi=116.0$ and 292.5 MeV ^{40,48}Ca$(\pi^\pm,\pi^\pm)$ data. The results are shown in Fig. 10. The elastic calculations with the energy shift (Figs. 11—18) are based on the ground-state densities given in Table IV and the energy shifts given in Tables V and VI. It is clear that the fits with the energy shift are far superior to those without it.

2. *Inelastic scattering analysis*

Inelastic scattering calculations were made using the ground-state proton point densities given in Table IV and equating the proton and neutron Fermi distribution parameters (Sec. IV B 2). The energy shifts used are given in Tables V and VI. For the transition densities, we used the same values as for the analysis of the $T_\pi=180.0$ MeV data. Additional transition densities for ^{40}Ca were obtained from fits to inelastic electron scattering data using an empirical shell model[26] and a Tassie model.[24] The data and resulting calculations for the $T_\pi=116.0$ MeV data are shown in Figs. 11—13, and for the $T_\pi=292.5$ MeV data in Figs. 14—18. The resulting neutron and proton transition strengths and $E2$ transition strengths[27] are listed in Tables II and III of Ref. 8. The absence of ^{42}Ca and ^{54}Fe data at $T_\pi=116.0$ MeV was owing to running time constraints during the experiment.

V. RESULTS

The ground-state neutron rms radii obtained from the fits are compared to theoretical calculations and to pro-

TABLE IX. Neutron rms radii of ^{42,44,48}Ca minus neutron rms radii of ^{40}Ca: $\langle r^2\rangle_n^{1/2}(^{42,44,48}\text{Ca})-\langle r^2\rangle_n^{1/2}(^{40}\text{Ca})$.

	DDHF[a] theory (fm)	(p,p')[b] 0.6, 1.0 GeV (fm)	(α,α')[c] 104 MeV (fm)	(π,π')[d] 130 MeV (fm)	Pionic[e] x rays (fm)	This experiment 116.0 MeV (fm)	180.0 MeV (fm)	292.5 MeV (fm)
^{42}Ca	0.08	0.06	0.085				0.01±0.05	0.01±0.05
^{44}Ca	0.14	0.11	0.141		0.05±0.05	0.09±0.12	0.16±0.06	0.17±0.10
^{48}Ca	0.23	0.20	0.298	0.30		0.16±0.11	0.18±0.06	0.23±0.04

[a]Obtained from Ref. 28 using a density-dependent Hartree-Fock calculation.
[b]Obtained from Ref. 29.
[c]Obtained from Ref. 30.
[d]Obtained from Refs. 1 and 2.
[e]Obtained from Refs. 3 and 4.

ton, alpha, and pion data analyses in Tables VII–IX. Table VII presents the neutron rms radii for ^{40,42,44,48}Ca taken from a density-dependent Hartree-Fock (DDHF) calculation,[28] $T_p=0.6$ and 1.0 GeV proton-scattering data,[29] $T_\alpha=104$ MeV alpha-scattering data,[30] and the data of this experiment. Table VIII presents the differences between the proton and neutron rms radii for ^{40,42,44,48}Ca, and Table IX presents the differences between the neutron rms radii of ^{42,44,48}Ca and the neutron rms radius of ^{40}Ca. Table IX also contains the analysis results of $T_\pi=130$ MeV pion data[1,2] and pionic x-ray data.[3,4]

The results from this experiment exhibit the same qualitative trends in going from ^{40}Ca to ^{48}Ca as do the other analyses. However, the neutron rms radii extracted at $T_\pi=116.0$ were larger than those extracted at 292.5 MeV, indicating an insufficiency in the model used in analyzing the elastic data. This discrepancy is in agreement with the predictions of Johnson and Bethe.[31] These authors discuss the difficulty in learning reliably about the low moments of the nucleon distribution, such as the rms radii, from the analysis of resonance energy experiments because pion scattering is primarily sensitive to the low-density part of the nuclear-density distribution. Their approach is to define an effective radius, and then to study changes in the value of the effective radius and changes in the nuclear density in the vicinity of the effective radius. Nevertheless, the quantitative agreement between the $T_\pi=180.0$ and 292.5 MeV data and the other analyses is an encouraging sign for the usefulness of pions in directly determining neutron distributions.

The empirical energy shift correction values obtained from the fits were -25.0 ± 4.0 MeV for the $T_\pi=116.0$ and 180.0 MeV data sets and -60.0 ± 9.0 MeV for the $T_\pi=292.5$ MeV data set. The value for ^{40}Ca obtained by Cottingame and Holtkamp[6] was -30.0 ± 4.0 MeV, which compares well with that obtained for the $T_\pi=116.0$ and 180.0 MeV data sets. It should be pointed out that the Cottingame and Holtkamp procedure fixed the neutron density distribution parameters to those of the proton, whereas, in this paper, the neutron density distribution parameters were allowed to be varied during the fitting process. Although a dramatic improvement in all fits owing to using the energy shift procedure was clearly evidenced, the anomalously large energy shift value obtained at $T_\pi=292.5$ MeV and the unusually large values for the neutron rms radii at $T_\pi=116.0$ indicate problems with the optical model near both the lower and upper energy regions of the $\Delta_{3,3}$ resonance. Nevertheless, with the large data base of calcium-isotope pion-scattering data now available and with an improved optical model, it should now be possible to determine whether or not neutron distributions can be unambiguously extracted from pion scattering by the calcium isotopes in particular and nuclei in general.

The analysis of the π^+ vs π^- differences in inelastic scattering to the low-lying collective states in ^{40,42,44,48}Ca and ^{54}Fe resulted in reasonable agreement with previous work. The transition strengths extracted in Ref. 8 from the $T_\pi=180.0$ MeV data also give a good description of both the $T_\pi=116.0$ and 292.5 MeV data presented here. The success in fitting the inelastic scattering data with a simple model with few free parameters suggests that pion scattering has a great potential for providing a general and powerful probe for addressing nuclear-structure problems.

This work was supported by the U.S. Department of Energy, the Robert A. Welch Foundation, and the National Science Foundation.

---

*Present address: Air Force Weapons Laboratory, Kirtland AFB, NM 87117.

†Present address: New Mexico State University, Las Cruces, NM 88003.

‡Present address: University of South Carolina, Columbia, SC 29208.

§Present address: Los Alamos National Laboratory, Los Alamos, NM 87545.

[1]J.-P. Egger, R. Corfu, P. Gretillat, C. Lunke, J. Piffaretti, E. Schwartz, C. Perrin, J. Jansen, and B. M. Preedom, Phys. Rev. Lett. 39, 1608 (1977).

[2]J.-P. Egger, in *Proceedings of the Karlsruhe International Discussion Meeting, What Do We Know About the Radial Shape of Nuclei in the Ca Region?,* edited by H. Rebel, H. J. Grils, and G. Schatz (Institüt für Angewandte Kernphysik, Karlsruhe, 1979), p. 270.

[3]C. J. Batty, S. F. Biagi, E. Friedman, S. D. Hoath, J. D. Davies, G. J. Pyle, G. T. A. Squier, D. M. Asbury, and M. Leon, Phys. Lett. 81B, 165 (1979).

[4]E. Friedman, see Ref. 2, p. 285.

[5]M. J. Jakobson, G. R. Burleson, J. R. Calarco, M. D. Cooper, D. C. Hagerman, I. Halpern, R. H. Jeppesen, K. F. Johnson, L. D. Knutson, R. E. Marrs, H. O. Meyer, and R. P. Redwine, Phys. Rev. Lett. 38, 1201 (1977).

[6]W. B. Cottingame and D. B. Holtkamp, Phys. Rev. Lett. 45, 1828 (1980).

[7]C. L. Morris, K. G. Boyer, C. Fred Moore, C. J. Harvey, K. J. Kallianpur, I. B. Moore, P. A. Seidl, S. J. Seestrom-Morris, D. B. Holtkamp, S. J. Greene, and W. B. Cottingame, Phys. Rev. C 24, 231 (1981).

[8]K. G. Boyer, W. B. Cottingame, L. E. Smith, S. J. Greene, C. Fred Moore, J. S. McCarthy, R. C. Minehart, J. F. Davis, G. R. Burleson, G. Blanpied, C. A. Goulding, H. A. Thiessen, and C. L. Morris, Phys. Rev. C 24, 598 (1981).

[9]H. A. Thiessen and S. Sobottka, Los Alamos Scientific Laboratory Report LA-4534-MS, 1970; H. A. Thiessen *et al.* (unpublished).

[10]L. G. Atenico, J. F. Amann, R. L. Boudrie, and C. L. Morris, Nucl. Instrum. Methods 187, 381 (1981); H. A. Thiessen *et al.* (unpublished).

[11]Kenneth Gary Boyer, Ph.D. dissertation, University of Texas at Austin, 1983.

[12]Lester Eugene Smith, computer program LOAF (unpublished).

[13]P. M. Endt and C. van der Leun, Nucl. Phys. A214, 444 (1973); A214, 491 (1973); A214, 533 (1973).

[14]Nucl. Data Sheets 23, 22 (1978); 23, 505 (1978).

[15]K. Witte, D. Dodder, and G. Hale, computer program EDA (unpublished).
[16]R. D. Sard, *Relativistic Mechanics* (Benjamin, New York, 1970), p. 241.
[17]R. A. Eisenstein and G. A. Miller, Comput. Phys. Commun. 11, 95 (1976).
[18]F. James and M. Roos, Comput. Phys. Commun. 10, 343 (1975).
[19]L. S. Kisslinger, Phys. Rev. 98, 761 (1955).
[20]G. Rowe, M. Salomon, R. H. Landau, Phys. Rev. C 18, 384 (1978).
[21]R. F. Frosch, R. Hofstadter, J. S. McCarthy, G. K. Noldeke, K. J. van Oostrum, M. R. Yearin, B. C. Clark, R. Herman, and D. G. Ravenhall, Phys. Rev. 174, 1380 (1963).
[22]A. S. Litvinenko, N. G. Shevchenko, A. Yu. Buki, G. A. Savitskii, V. M. Khvastunov, and R. L. Kondrat'ev, Yad. Fiz. 14, 40 (1971) [Sov. J. Nucl. Phys. 14, 23 (1972)].
[23]G. S. Adams, T. S. Bauer, G. Igo, G. W. Hoffmann, G. R. Smith, and M. Gazzaly, Phys. Rev. C 21, 2485 (1980).
[24]P. L. Hollowell, W. Bertozzi, J. Heisenberg, S. Kowalski, X. Maruyama, C. P. Sargent, W. Turchinetz, C. F. Williamson, S. P. Fivozinsky, J. W. Lightbody, and S. Penner, Phys. Rev. C 7, 1396 (1973).
[25]R. A. Eisenstein, D. W. Madsen, H. Thiessen, L. S. Cardman, and C. K. Bockelman, Phys. Rev. 188, 1815 (1969).
[26]K. Itoh, M. Oyamada, and Y. Torizuka, Phys. Rev. C 2, 2181 (1970).
[27]P. M. Endt, At. Data Nucl. Data Tables 32, 3 (1979); 32, 547 (1979).
[28]X. Campi, see Ref. 2, p. 362.
[29]I. Brissaud and X. Campi, see Ref. 2, p. 195.
[30]H. J. Gils, see Ref. 2, p. 123.
[31]M. B. Johnson and H. A. Bethe, Comments Nucl. Part. Phys. 8, 75 (1978).